Micron 43 (2012) 30–36

Contents lists available at ScienceDirect

Micron

journal homepage: www.elsevier.com/locate/micron

Distinguishing the core from the shell in MnO_x/MnO_y and FeO_x/MnO_x core/shell nanoparticles through quantitative electron energy loss spectroscopy (EELS) analysis

S. Estradé[a,b,*], Ll. Yedra[a], A. López-Ortega[c], M. Estrader[c], G. Salazar-Alvarez[d], M.D. Baró[e], J. Nogués[c,f], F. Peiró[a]

[a] LENS, MIND-IN2UB, Departament d'Electrònica, Universitat de Barcelona, Martí i Franquès 1, 08028 Barcelona, Spain
[b] TEM-MAT, CCiT, Universitat de Barcelona, Solé i Sabarís 1, 08028 Barcelona, Spain
[c] CIN2 (ICN-CSIC) and Universitat Autònoma de Barcelona, Catalan Institute of Nanotechnology, Campus de la UAB, 08193 Bellaterra (Barcelona), Spain
[d] Department of Materials and Environmental Chemistry, Arrhenius Laboratory, Stockholm University, 10691 Stockholm, Sweden
[e] Departament de Física, Universitat Autònoma de Barcelona, 08193 Bellaterra, Spain
[f] Institució Catalana de Recerca i Estudis Avançats (ICREA), Barcelona, Spain

ARTICLE INFO

Article history:
Received 25 February 2011
Received in revised form 26 March 2011
Accepted 11 April 2011

Keywords:
EELS
Mn-oxide
Fe-oxide
Core–shell
Nanoparticles

ABSTRACT

The structural and chemical characterization of inverted bi-magnetic MnO_x(antiferromagnetic)/MnO_y(ferrimagnetic) and FeO_x(soft-ferrimagnetic)/MnO_x(hard-ferrimagnetic) core/shell nanoparticles has been carried out by means of scanning transmission electron microscopy with electron energy loss spectroscopy analysis, (S)TEM-EELS. Quantitative EELS was applied to assess the local composition of the nanoparticles by evaluating the local Mn oxidation state based on the Mn L_3/L_2 peak intensity ratio and the Mn L_3 peak onset. The analysis allows to unambiguously distinguish the core from the shell and to determine the nature of the involved manganese oxides in both cases. The results evidence that the structure of the nanoparticles is, in fact, more complex than the one designed by the synthesis parameters.

1. Introduction

Bi-magnetic core/shell nanoparticles are gaining increased interest in recent years due to their novel properties and because of their potential application in diverse fields (e.g., magnetic recording, hard magnets, sensors or biomedical applications). Mainly two different kinds of system can be distinguished, those involving ferromagnets (FM), or ferrimagnets (FiM), and antiferromagnets (AM) and those involving solely FM and/or FiM, although with different anisotropies, i.e., soft and hard. In the case involving AFMs, the exchange coupling between the FM and AFM phases [i.e., exchange bias (Nogués et al., 2005)] has been shown to lead to enhanced coercivities (Sort et al., 2001, 2002) and improved superparamagnetic blocking temperatures (Skumryev et al., 2003; Eisenmenger and Schuller, 2003). Interestingly, most of the studies involving AFMs are based on the partial oxidation of FM transition metal magnetic particles, where many of their oxides are AFM, leading to a FM core/AFM shell structure. Some examples of this simple procedure are Co/CoO, Co_3O_4 (Nogués et al., 2006), Ni/NiO (Löffler et al., 1998), NiCo/NiCoO (Luna et al., 2004), FeCo/FeCoO (Ennas et al., 2004), Fe/Fe_3O_4, γ-Fe_2O_3, α-Fe_2O_3, and FeO—note that Fe_3O_4 and γ-Fe_2O_3 are ferrimagnetic (del Bianco et al., 2004). On the other hand, studies involving "inverted" structures, i.e., composed of an AFM core and a FiM shell, are rather scarce. In this case, MnO–Mn_3O_4 (Salazar-Alvarez et al., 2007b; Golosovsky et al., 2009; Berkowitz et al., 2008) and FeO–Fe_3O_4 (Kavich et al., 2008; Redl et al., 2004; Hai et al., 2010) are the most studied systems. Concerning, the core/shell systems involving only hard/soft FM and/or FiM counterparts, the exchange coupling between the two phases has been shown to result in exchange spring effects (Kneller and Hawig, 1991) leading to improved energy products, similar to what is observed in thin film systems (Fullerton et al., 1999). In this case the most studied structure is formed by a hard core and a soft shell, e.g., FePt/Fe_3O_4 (Nandwana et al., 2009; Zeng et al., 2004), $CoFe_2O_4$/$ZnFe_2O_4$ (Masala et al., 2006) or Sm($Co_{1-x}Fe_x$)|Fe_3O_4 (Hong et al., 2007). However, a few studies involving "inverted" structures, i.e., having a soft core and a hard shell, have also been reported (Zeng et al., 2004; Masala et al., 2006; Salazar-Alvarez et al., 2007a; Cheon et al., 2006).

* Corresponding author at: LENS, MIND-IN2UB, Departament d'Electrònica, Universitat de Barcelona, Martí i Franquès 1, 08028 Barcelona, Spain.
Tel.: +34 934021695; fax: +34 934021148.
E-mail address: sestrade@ub.edu (S. Estradé).

0968-4328/$ – see front matter © 2011 Elsevier Ltd. All rights reserved.
doi:10.1016/j.micron.2011.04.002

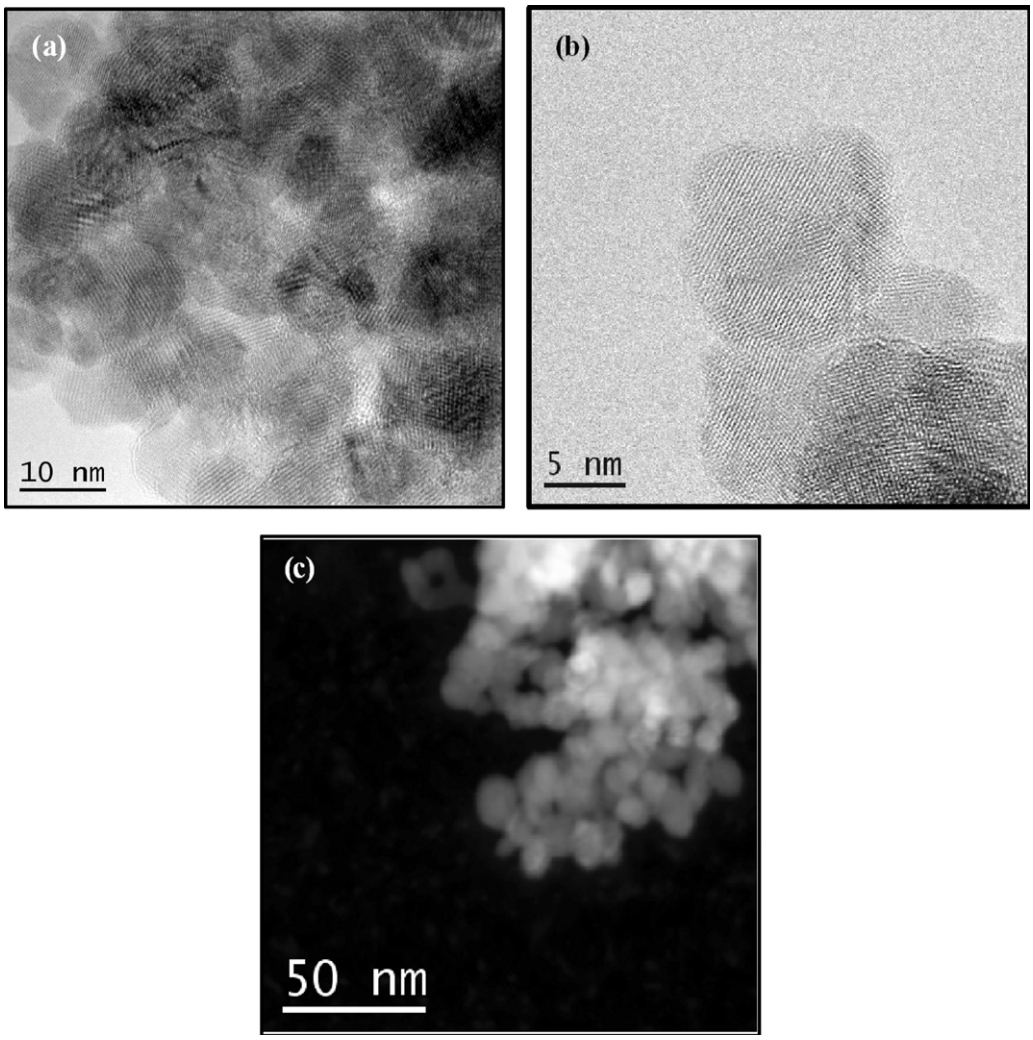

Fig. 1. HRTEM (a), (b) and HAADF (c) images of several MnO_x/MnO_y core/shell nanoparticles.

Notably, many of the studied bimagnetic core/shell systems (AFM/FiM and FiM/FiM) involve either the same or similar transition metal ions, with comparable crystal structures, in the core and the shell. This often makes the clear determination of the core/shell structure rather challenging. For example, high resolution TEM does not allow distinguishing between the core and the shell in systems where the shell grows epitaxially on the core. Similarly, high angle annular dark field (HAADF) imaging does not yield any distinguishable contrast for systems where the *Z* numbers are exceedingly close. Thus, since the core diameter and the shell thickness control the magnetic properties of these materials, quantitative tools to assess this type of structures are highly desirable.

Here we present the determination of the core/shell structure of two different types of "inverse" core/shell nanoparticles, i.e., MnO_x/MnO_y, (AFM/FiM) and FeO_x/MnO_x (soft-FiM/hard-FiM) using quantitative EELS analysis. The results demonstrate that not only that the core and shell morphology can be univocally established but also the possibility to quantitatively determine the precise oxidation state of the Mn ions. The analysis shows that structures can be more complex than the expected homogeneous core/shell, exhibiting for example multiphase onion-type structures or asymmetric shapes.

2. Materials and methods

The MnO_x/MnO_y nanoparticles were prepared by thermolysis of manganese (II) acetylacetonate leading, nominally, to a MnO AFM-core which after passivation under air yields to the corresponding ferrimagnetic Mn_3O_4 shell (López-Ortega et al., 2010).

The synthesis of core/shell FeO_x/MnO_x particles was carried out following a multi-step procedure where preformed iron oxide nanoparticles were used as seeds for the subsequent growth of manganese oxide and its passivation. Briefly, the iron oxide seeds were prepared by thermolysis of the iron (III) oleate nominally leading to soft-ferrimagnetic Fe_3O_4 nanoparticles. The hard-ferrimagnetic Mn_3O_4 layers were then laid by thermolysis of manganese (II) acetylacetonate using the Fe_3O_4 nanoparticles as seeds (Salazar-Alvarez et al., submitted for publication).

Nanoparticles for scanning transmission electron microscopy with electron energy loss spectroscopy, (S)TEM-EELS, analyses were deposited on carbon coated copper grids.

TEM-EELS measurements were carried out using a JEOL 2010F field emission gun (S)TEM, working at 200 kV with a point-to-point resolution of 0.19 nm, and equipped with a postcolumn Gatan Image Filter (GIF) energy spectrometer.

EEL spectra were acquired at about every 0.5 nm along the diameter of the nanoparticles at an energy range containing the Mn-$L_{2,3}$,

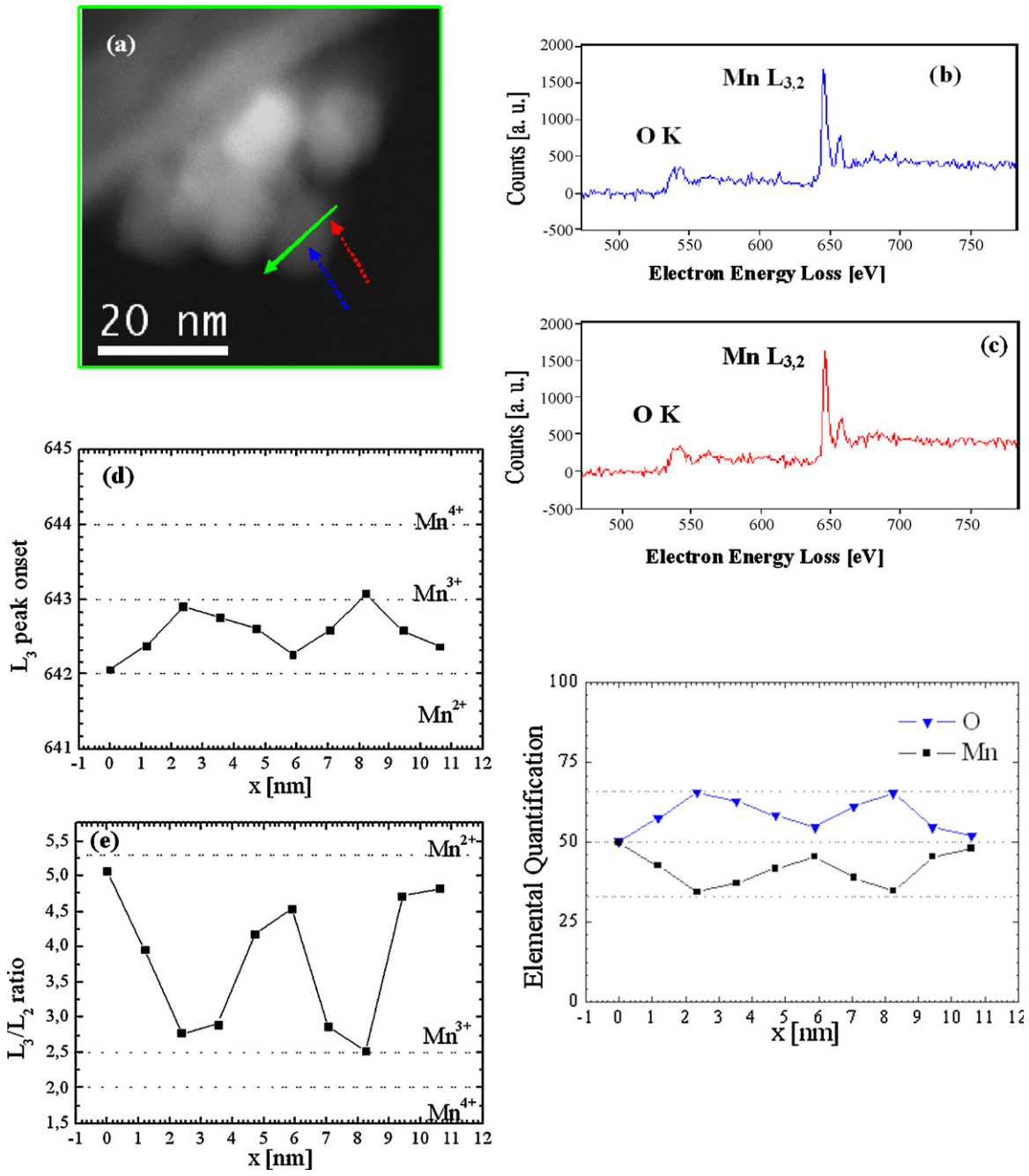

Fig. 2. (a) HAADF image of several nanoparticles. (b and c) Background-subtracted EEL spectra obtained at the positions indicated in (a), dotted arrows. (d) Mn L_3 peak position along the thick arrow highlighted in (a). (e) Mn L_3/L_2 intensity ratio along the line highlighted in (a). (f) Elemental quantification along the line highlighted in (a).

Fe-$L_{2,3}$ and the O–K edges, with an energy resolution of 0.8 eV. The used probe size was 0.5 nm, convergence and collection semiangles were 9 rad and 10 rad, respectively, and the acquisition time was of 5 s for each spectrum. Longer acquisition times were tested to evaluate the degree of beam sensitivity of the samples: samples were not found to be beam sensitive for acquisition times under 20 s; otherwise, a reduction, and an eventual piercing of the nanoparticles was observed.

Notice that several particles were measured for each sample.

3. Calculations

Elemental quantification calculations were carried out by the standard procedure of comparing the cross-section weighted, background subtracted, integrated signals, using Digital Micrograph.

Regarding the determination of Mn oxidation state, it has been reported (Kurata and Colliex, 1993; Garvie and Craven, 1994; Schmid and Mader, 2006) that both the Mn L_3 peak onset and the Mn L_3/L_2 intensity ratio are measures of the Mn oxidation state. Thus, to obtain the Mn oxidation state of the nanoparticles the values obtained from the experimental spectra are compared to reference experimental values from the literature (Kurata and Colliex, 1993; Garvie and Craven, 1994; Schmid and Mader, 2006).

In practice, first the spectra at the nanoparticle are deconvoluted from the low-loss spectrum (obtained in the same region) to eliminate multiple scattering using Digital Micrograph. Subsequently, after correcting the energy scale and subtracting the pre-peak background and the continuum contributions, the experimental Mn L_3 peak onset and the Mn L_3/L_2 intensity ratio are obtained. These values are then compared to the reference literature values. Given the

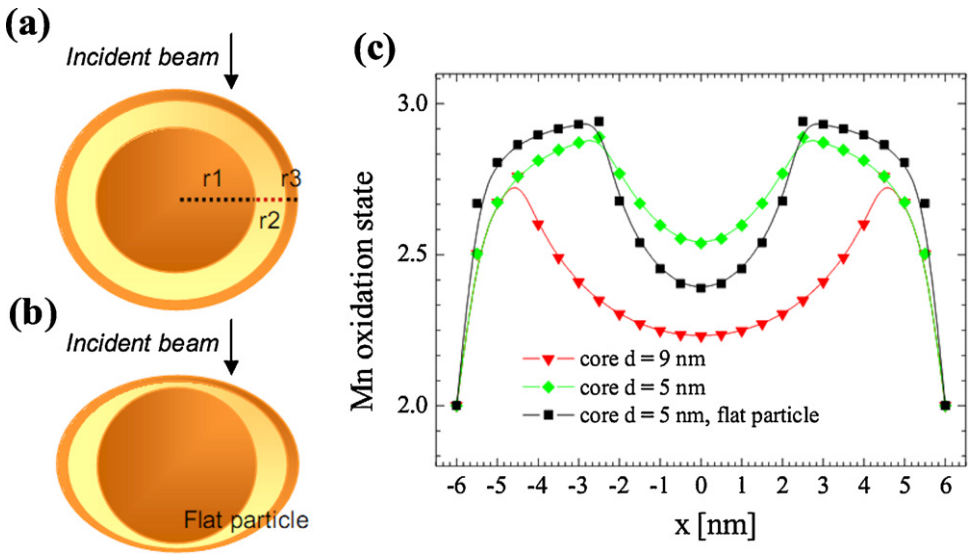

Fig. 3. Schematic representation of a nanoparticle, considered to be spherical (a), or flat (b). Simulated results of the spatial distribution of Mn oxidation state (c).

tedious procedure, a Matlab-based software package, "Manganitas" (Estradé et al., 2007, 2008, 2009), has been developed to carry out the calculation in a systematic manner. The software locates a reference edge and recalibrates the energy axis of each individual spectrum using this edge as a reference. Then, it fits the pre-peak background using a power-law fit function and subtracts it. Transitions to continuum are fitted via a step function and subtracted as well—this latter step is critical, as thickness changes necessarily

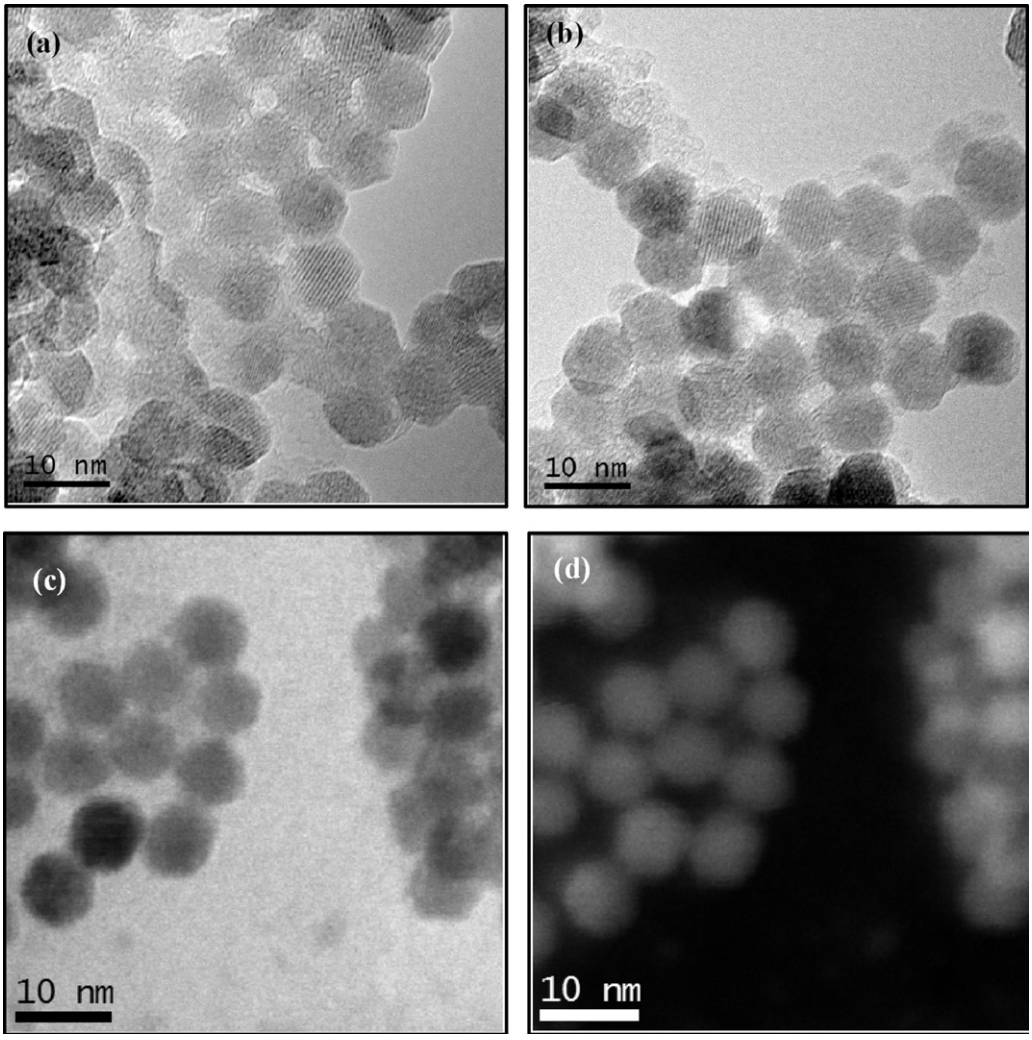

Fig. 4. HRTEM (a), (b), BF-STEM (c) and HAADF (d) images of several FeO_x/MnO_x core/shell nanoparticles.

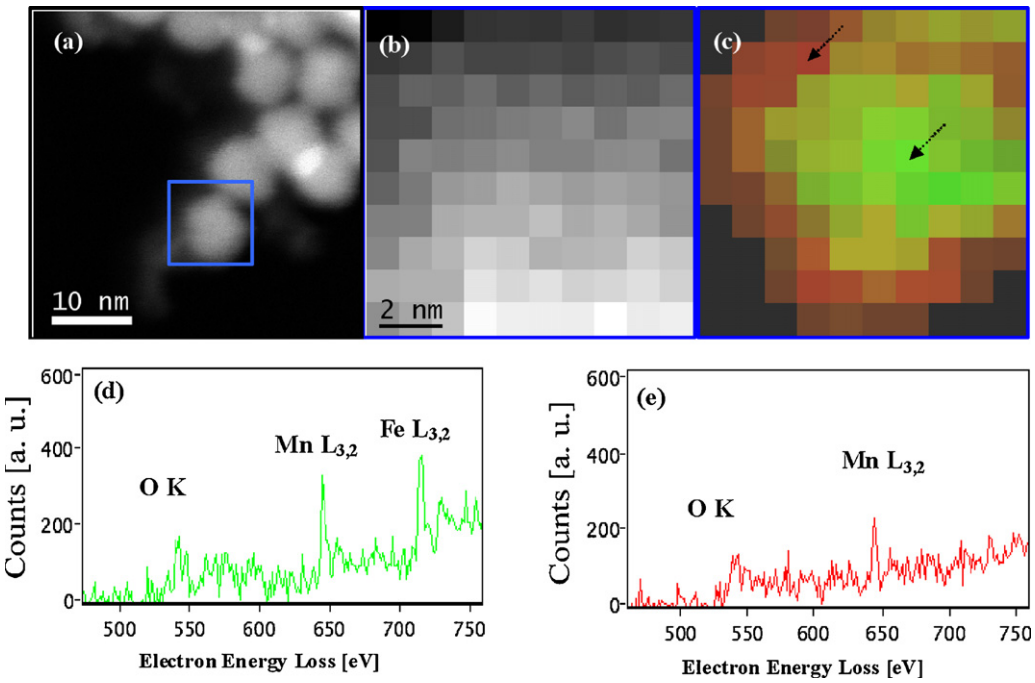

Fig. 5. (a) HAADF image of several core–shell nanoparticles. (b) Spectrum image obtained in the highlighted zone in (a). Chemical mapping obtained by MLLS fitting of (b) using spectra (d) and (e) as a reference—it can be understood as a mapping of the regions containing both Fe and Mn (green) and Mn only (red). (d and e) EEL spectra obtained at the indicated points in (c). (For interpretation of the references to color in this figure legend, the reader is referred to the web version of the article.)

along the nanoparticles. Gaussian curves are fitted to both Mn L_3 and Mn L_2 peaks. The Mn L_3 onset is established to be at half the height of the peak. The area under the Gaussian curves (I_3 and I_2) is integrated and I_3/I_2 is calculated.

Notice that the relative error in the determination of the L_3 peak chemical shift and the L_3/L_2 intensity ratio (and consequently the Mn-oxidation state and elemental quantification) are estimated to be about 5%.

4. Results and discussion

4.1. MnO_x/MnO_y

HRTEM and STEM observations showed that the nanoparticles are about 14 nm in diameter (López-Ortega et al., 2010), as illustrated in Fig. 1. As expected, it was not possible to distinguish between core and shell in the HAADF images (Fig. 1(c)), since the difference between the mean Z of two Mn oxides is not enough to resolve it. Similarly, since in this system the shell grows epitaxially on the core (Berkowitz et al., 2008) the core/shell structure is not evident in the HRTEM images in Fig. 1(a) and (b).

EEL spectra were obtained for several nanoparticles along their diameter (as shown schematically in Fig. 2(a) by a thick arrow). Two examples of spectra taken at different positions (as shown by dotted arrows in Fig. 2(a)) are shown in Fig. 2(b) and (c). The quantitative analysis of the results is shown in Fig. 2(d) and (e) for one of the particles, although the different studied particles were found to be consistent with each other.

From the elemental quantification (Fig. 2(e)) an MnO core is clearly observed (even if, when obtaining an EELS signal from the centre of a nanoparticle, the signal arises both from the core and the enveloping layer, making it impossible to obtain a pure MnO spectrum). As for the shell, it is apparent from EELS data that it consists of two parts: an inner Mn_2O_3 layer and a very thin outer MnO layer. It thus seems that the particles have a $MnO/Mn_2O_3/MnO$ radial, onion-like, structure. The central layer is clearly not Mn_3O_4, as the data in Fig. 2 strongly suggest the presence of an Mn^{3+} phase, in agreement with recent magnetic results on similar samples (López-Ortega et al., 2010).

In order to gain further insight into the structure, we have calculated (Fig. 3), from simple geometric considerations, the total projected EELS signal that would be obtained for a nanoparticle starting with the structure MnO (r1 = 4.5 nm)/Mn_2O_3 (r2 = 1.5 nm)/MnO (r3 = 0.5 nm). Since the simulation was still far from the experimental results, the core diameter and the radius of the inner shell were optimized. The best correlation between experimental and calculated data is obtained for an intermediate layer of r2 = 3.5 nm and a core radius of r1 = 2.5 nm. Moreover, taking into account that the nanoparticles do not seem to be perfectly spherical, an even better agreement with experimental data can be obtained when considering (in a somewhat arbitrary way) that the outer layers are half in thickness in the direction perpendicular to the beam compared to the in-plane directions (thus considering a flat particle).

The results clearly indicate that the nanoparticles are far more complex than the originally designed MnO/Mn_3O_4. As discussed by López-Ortega et al. (2010) the origin of the Mn_2O_3 phase (rather than Mn_3O_4) may arise from the size of the core, which due to defects, may favour the growth of Mn_2O_3. The presence of an outer shell of MnO is less clear, although it may be due to the reducing effect of the surfactant layer covering the particles.

4.2. FeO_x/MnO_y

HRTEM observation of the FeO_x/MnO_x nanoparticles yielded a mean particle diameter of 7.9 nm, with a standard deviation of 0.7 nm (Fig. 4(a) and (b)). Since the Fe_3O_4 seeds were found to have a 6.5 nm diameter (not shown), the grown shell is determined to be about 0.7 nm thick. Bright field-STEM (BF-STEM) and HAADF images of several nanoparticles are also given in Fig. 4(c) and (d), respectively. No diffraction contrast between core and shell is observed in BF-STEM. As Mn and Fe have very close Z numbers (Z = 25 and Z = 26, respectively), no contrast is found in HAADF either.

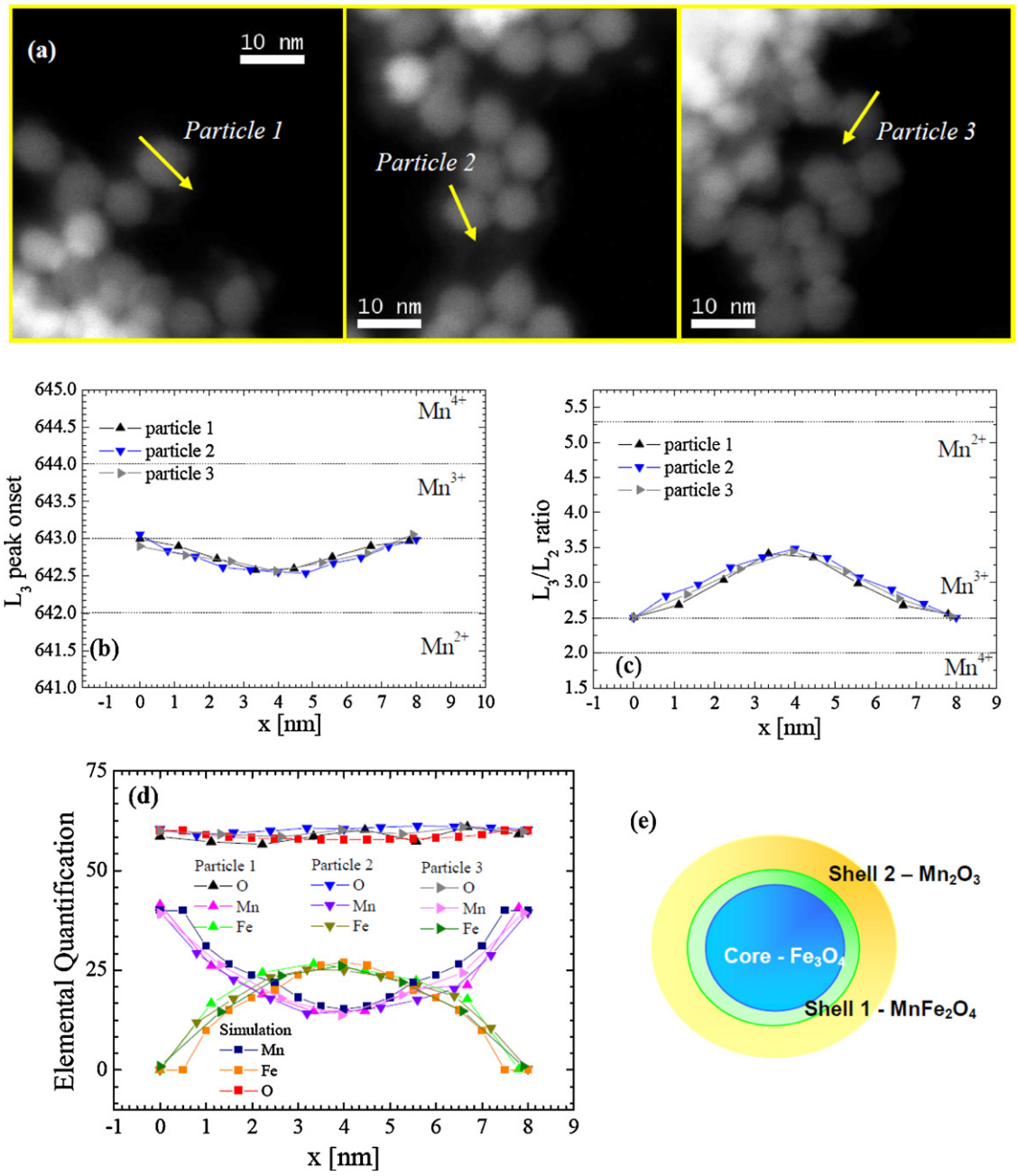

Fig. 6. (a) HAADF images of several core–shell nanoparticles. (b) L_3 peak position and (c) Mn L_3/L_2 intensity ratio along the lines highlighted in the HAADF images, for the three considered nanoparticles. (d) Elemental quantification for the three considered particles, and simulation considering a 2 nm thick an $MnFe_2O_4$ spinel around a Fe_3O_4 core. (e) Cartoon of the structure of the nanoparticles.

From the EEL spectra at different positions we have constructed a 2D EELS spectrum image (see Fig. 5(b)) of the core/shell nanoparticle highlighted in Fig. 5(a). By using multiple linear least square (MLLS) fits of the spectrum image we have constructed a 2D chemical mapping (Fig. 5(c)). Interestingly, this chemical fingerprinting makes it already possible to distinguish between a shell, where only Mn signal is observed (see Fig. 5(e)), and a core, where both (projected) Mn and Fe signals are found (see Fig. 5(d)).

Further, quantitative EELS analysis has been carried out to better understand the structure of the nanoparticles. EELS data obtained from spectrum lines across several nanoparticles (highlighted in Fig. 6(a)) show that the Mn oxidation state is 3+ at the outer part of the particles (i.e., where no Fe signal is found) and decreases moderately towards the centre of the particles (Fig. 6(b) and (c)). Mn, Fe and O elemental quantification through several nanoparticles (also given in Fig. 6) evidences the pure MnO_y outer layer to be about 1 nm thick. In addition, it is clear from elemental quantification data that there must be some additional Mn towards the core of the nanoparticles. Thus, the presence of a mixed phase containing Mn, Fe and O must be considered. Both an $MnFe_2O_4$ and a $FeMn_2O_4$ middle layer seem plausible. Taking the composition and the thickness of the mixed phase and the composition of the Fe and Mn oxides (Fe_3O_4 seeds and MnO_x outer shell, respectively) as parameters to simulate the experimental projected EELS data, the best agreement has been achieved for an $MnFe_2O_4$ spinel about 2 nm thick around a Fe_3O_4 core (Fig. 6(e)). Consequently, the overall system would then correspond to tri-magnetic, hetero-onion, nanoparticles composed by core-Fe_3O_4 (5 nm)/shell1-$MnFe_2O_4$ (2 nm)/shell2-Mn_2O_3 (1 nm).

Similar to what was observed for the MnO_x/MnO_y system, the structure of the particle also differs from the designed one (i.e., Fe_3O_4/Mn_3O_4). In this case the discrepancy in the structure seems to arise from the diffusion of Mn ions from the outer shell towards the core during the synthesis. This leads to the depletion of Mn from the outer layer and the formation of a mixed intermediate layer.

5. Conclusions

The composition of MnO_x/MnO_y and FeO_x/MnO_x nanoparticles was determined by STEM-EELS. The obtained morphologies exhibit an onion-type structure, $MnO/Mn_2O_3/MnO$ and $Fe_3O_4/MnFe_2O_4/Mn_2O_3$, in contrast to the designed MnO/Mn_3O_4 and Fe_3O_4/Mn_3O_4 core/shell morphologies. Furthermore, in the MnO_x/MnO_y case the results hint a possible shape anisotropy in the particles. This study highlights the power of quantitative EELS analysis to resolve core/shell structures even in cases where HRTEM or HAADF cannot distinguish them.

Acknowledgements

The authors acknowledge the financial support by the Spanish Government (IMAGINE-Consolider, SOLEMN and MAT2010-20616-C02 projects), the Catalan Government (2009-SGR-1292) and the TEM facilities of Science and Technical Centers of Universitat de Barcelona (CCiT-UB).

References

Berkowitz, A.E., Rodriguez, G.F., Hong, J.I., An, K., Hyeon, T., Agarwal, N., Smith, D.J., Fullerton, E.E., 2008. Antiferromagnetic MnO nanoparticles with ferrimagnetic Mn_3O_4 shells: doubly inverted core–shell system. Phys. Rev. B 77, 024403.

Cheon, J., Park, J.-I., Choi, J.-S., Jun, Y.-W., Kim, S., Kim, M.G., Kim, Y.-M., Kim, Y.J., 2006. Magnetic superlattices and their nanoscale phase transition effects. Proc. Natl. Acad. Sci. U.S.A. 103, 3023.

del Bianco, L., Fiorani, D., Testa, A.M., Bonetti, E., Signorini, L., 2004. Field-cooling dependence of exchange bias in a granular system of Fe nanoparticles embedded in an Fe oxide matrix. Phys. Rev. B 70, 052401.

Eisenmenger, J., Schuller, I.K., 2003. Magnetic nanostructures: overcoming thermal fluctuations. Nat. Mater. 2, 437.

Ennas, G., Falqui, A., Marras, S., Sangregorio, C., Marongiu, G., 2004. Influence of metal content on size, dispersion, and magnetic properties of iron–cobalt alloy nanoparticles embedded in silica matrix. Chem. Mater. 16, 5659.

Estradé, S., Arbiol, J., Peiró, F., Abad, L., Laukhin, V., Balcells, L., Martínez, B., 2007. Cationic diffusion in $La_{2/3}Ca_{1/3}MnO_3$ thin films grown on $LaAlO_3$ (0 0 1) substrates. Appl. Phys. Lett. 91, 252503.

Estradé, S., Arbiol, J., Peiró, F., Infante, I.C., Sánchez, F., Fontcuberta, J., de la Peña, F., Walls, M., Colliex, C., 2008. Cationic and charge segregation in $La_{2/3}Ca_{1/3}MnO_3$ thin films grown on (0 0 1) and (1 1 0) $SrTiO_3$. Appl. Phys. Lett. 93, 112505.

Estradé, S., Rebled, J.M., Arbiol, J., Peiró, F., Infante, I.C., Herranz, G., Sánchez, F., Fontcuberta, J., Córdoba, R., Mendis, B.G., Bleloch, A.L., 2009. Effects of thickness on the cation segregation in epitaxial (0 0 1) and (1 1 0) $La_{2/3}Ca_{1/3}MnO_3$ thin films. Appl. Phys. Lett. 95, 072507.

Fullerton, E.E., Jiang, J.S., Bader, S.D., 1999. Hard/soft magnetic heterostructures: model exchange-spring magnets. J. Magn. Magn. Mater. 200, 392.

Garvie, L.A.J., Craven, A.J., 1994. Electron-beam-induced reduction of Mn4+ in manganese oxides as revealed by parallel EELS. Ultramicroscopy 54, 83.

Golosovsky, I.V., Salazar-Alvarez, G., López-Ortega, A., Gonzalez, M.A., Sort, J., Estrader, M., Suriñach, S., Baró, M.D., Nogués, J., 2009. Magnetic proximity effect features in antiferromagnetic/ferrimagnetic core–shell nanoparticles. Phys. Rev. Lett. 102, 247201.

Hai, H.T., Yang, H.T., Kura, H., Hasegawa, D., Ogata, Y., Takahashi, M., Ogawa, T., 2010. Size control and characterization of wustite (core)/spinel (shell) nanocubes obtained by decomposition of iron oleate complex. J. Colloid Interface Sci. 346, 37.

Hong, J.H., Kim, W.S., Lee, J.I., Hur, N.H., 2007. Exchange coupled magnetic nanocomposites of $Sm(Co_{1-x}Fe_x)_5/Fe_3O_4$ with core/shell structure. Solid State Commun. 141, 541.

Kavich, D.W., Dickerson, J.H., Mahajan, S.V., Hasan, S.A., Park, J.-H., 2008. Exchange bias of singly inverted FeO/Fe_3O_4 core–shell nanocrystals. Phys. Rev. B 78, 174414.

Kneller, E.F., Hawig, R., 1991. The exchange spring magnet—a new material principle for permanent magnets. IEEE Trans. Magn. 27, 3588.

Kurata, H., Colliex, C., 1993. Electron-energy-loss core-edge structures in manganese oxides. Phys. Rev. B 48, 2102.

Löffler, J.F., Meier, J.P., Doudin, B., Ansermet, J.P., 1998. Random and exchange anisotropy in consolidated nanostructured Fe and Ni: role of grain size and trace oxides on the magnetic properties. Phys. Rev. B 57, 2915.

López-Ortega, A., Tobia, D., Winkler, E., Golosovsky, I.V., Salazar-Álvarez, G., Estradé, S., Estrader, M., Sort, J., González, M.A., Suriñach, S., Arbiol, J., Peiró, F., Zysler, R.D., Baró, M.D., Nogués, J., 2010. Size-dependent passivation shell and magnetic properties in antiferromagnetic/ferrimagnetic core/shell MnO nanoparticles. J. Am. Chem. Soc. 132, 9398.

Luna, C., del Puerto Morales, M., Serna, C.J., Vázquez, M., 2004. Exchange anisotropy in $Co_{80}Ni_{20}$/oxide nanoparticles. Nanotechnology 15, S293.

Masala, O., Hoffman, D., Sundaran, N., Page, K., Proffen, T., Lawes, G., Seshadri, R., 2006. Preparation of magnetic spinel ferrite core/shell nanoparticles: soft ferrites on hard ferrites and vice versa. Solid State Sci. 8, 1015.

Nandwana, V., Chaubey, G.S., Yano, K., Rong, C.-B., Liu, J.P., 2009. Bimagnetic nanoparticles with enhanced exchange coupling and energy products. J. Appl. Phys. 105, 014303.

Nogués, J., Skumryev, V., Sort, J., Stoyanov, S., Givord, D., 2006. Shell-driven magnetic stability in core–shell nanoparticles. Phys. Rev. Lett. 97, 157203.

Nogués, J., Sort, J., Langlais, V., Skumryev, V., Suriñach, S., Muñoz, J.S., Baró, M.D., 2005. Exchange bias in nanostructures. Phys. Rep. 422, 65.

Redl, F.X., Black, C.T., Papaefthymiou, G.C., Sandstrom, R.L., Yin, M., Zeng, H., Murray, C.B., O'Brien, C.B., 2004. Magnetic, electronic, and structural characterization of nonstoichiometric iron oxides at the nanoscale. J. Am. Chem. Soc. 126, 14583.

Salazar-Alvarez, G., Sort, J., Uheida, A., Muhammned, M., Suriñach, S., Baró, M.D., Nogués, J., 2007a. Reversible post-synthesis tuning of the superparamagnetic blocking temperature of γ-Fe_2O_3 nanoparticles by absorption and desorption of Co(II) ions. J. Mater. Chem. 17, 322.

Salazar-Alvarez, G., Sort, J., Suriñach, S., Baro, M.D., Nogues, J., 2007b. Synthesis and size-dependent exchange bias in inverted core–shell $MnO|Mn_3O_4$ nanoparticles. J. Am. Chem. Soc. 129, 9102.

Salazar-Alvarez, G., Lidbaum, H., López-Ortega, A., Estrader, M., Leifer, K., Sort, J., Suriñach, S., Baró, M.D., Nogués, J., submitted for publication.

Schmid, H.K., Mader, W., 2006. Oxidation states of Mn and Fe in various compound oxide systems. Micron 37, 426.

Skumryev, V., Stoyanov, S., Zhang, Y., Hadjipanayis, G., Givord, D., Nogués, J., 2003. Beating the superparamagnetic limit with exchange bias. Nature 423, 850.

Sort, J., Nogués, J., Suriñach, S., Muñoz, J.S., Baró, M.D., Chappel, E., Dupont, F., Chouteau, G., 2001. Coercivity and squareness enhancement in ball-milled hard magnetic–antiferromagnetic composites. Appl. Phys. Lett. 79, 1142.

Sort, J., Suriñach, S., Muñoz, J.S., Baró, M.D., Nogués, J., Chouteau, G., Skumryev, V., Hadjipanayis, G.C., 2002. Improving the energy product of hard magnetic materials. Phys. Rev. B 65, 174420.

Zeng, H., Sun, S., Li, J., Wang, Z.L., Liu, J.P., 2004. Tailoring magnetic properties of core/shell nanoparticles. Appl. Phys. Lett. 85, 792.